










HST SHEL: Revealing Haze and Confirming Elevated Metallicity in the Warm Neptune HAT-P-26b

LAKEISHA M. RAMOS ROSADO ¹, DAVID K. SING ^{1,2}, NATALIE H. ALLEN ¹, HANNAH R. WAKEFORD ³,
MERCEDES LÓPEZ-MORALES ⁴, NIKOLAY K. NIKOLOV ⁴, KEVIN B. STEVENSON ⁵, MUNAZZA K. ALAM ⁴ AND
THOMAS M. EVANS-SOMA ^{6,7}

¹*William H. Miller III Department of Physics and Astronomy, Johns Hopkins University, 3400 N. Charles Street, Baltimore, MD 21218, USA*

²*Department of Earth and Planetary Sciences, Johns Hopkins University, 3400 N. Charles Street, Baltimore, MD 21218, USA*

³*School of Physics, University of Bristol, HH Wills Physics Laboratory, Tyndall Avenue, Bristol BS8 1TL, UK*

⁴*Space Telescope Science Institute, 3700 San Martin Drive, Baltimore, MD 21218, USA*

⁵*Johns Hopkins APL, 11100 Johns Hopkins Rd, Laurel, MD 20723, USA*

⁶*School of Information and Physical Sciences, University of Newcastle, Callaghan, NSW, Australia*

⁷*Max Planck Institute for Astronomy, Königstuhl 17, D-69117 Heidelberg, Germany*

ABSTRACT

We present a new and extended transmission spectrum of the warm Neptune HAT-P-26b spanning wavelengths between 0.29 – 5.0 μm . This spectrum is derived from new HST STIS G430L observations from the PanCET program, a reanalysis of the previously published HST STIS G750L data, along with the previously published HST WFC3 IR G102 and G141 data, and the two Spitzer IRAC photometric points at 3.6 and 4.5 μm . We present this analysis as part of the Sculpting Hubble’s Exoplanet Legacy (SHEL) program, where the goals are to analyze all HST archival observations of transiting exoplanets using a uniform and homogeneous reduction technique. With the new wavelength coverage, we identify a scattering slope that is weaker than Rayleigh scattering and is best-matched by models incorporating a haze-only scenario. Our retrieval analysis reveals an atmospheric metallicity of $15_{-8}^{+22} \times$ solar which suggests that HAT-P-26b may have formed further out in the protoplanetary disk, in a region rich in hydrogen and helium but with fewer heavy elements, and later migrated inward. This super-solar metallicity places HAT-P-26b below the mass-metallicity trend of the solar system. Looking ahead, recent observations from JWST NIRISS/SOSS and NIRSpec/G495H will provide critical, high-precision data that extend the spectral coverage into the infrared to further constrain the atmospheric composition and structure of HAT-P-26b. These observations have the potential to confirm or refine the metallicity and haze scenario presented here, offering unprecedented insights into the atmospheric properties of warm Neptunes and the processes governing their formation and migration histories.

Keywords: planets and satellites: atmospheres — planets and satellites: individual (HAT-P-26b) — techniques: spectroscopic

1. INTRODUCTION

Over the past two decades, transmission spectroscopy observations with the *Hubble Space Telescope* (HST) have proven highly successful in exploring the atmospheres of giant planets, resulting in the detection of multiple species. Some notable highlights from HST include detection of atomic species (e.g., Charbonneau

et al. 2002; Vidal-Madjar et al. 2003; Sing et al. 2011; Huitson et al. 2013; Nikolov et al. 2014; Ehrenreich et al. 2015; Sing et al. 2016; Alam et al. 2018; Sing et al. 2019; Carter et al. 2020; Alam et al. 2021; Nikolov et al. 2022) as well as clouds and hazes (Lecavelier Des Etangs et al. 2008; Bean et al. 2010; Sing et al. 2013; Kreidberg et al. 2014a; Sing et al. 2016; Kirk et al. 2017; Wakeford et al. 2017b; Alam et al. 2018; Benneke et al. 2019; Gao et al. 2020; Rathcke et al. 2023; Changeat et al. 2024) and molecular detections (e.g., Deming et al. 2013; Wake-

ford et al. 2013; Kreidberg et al. 2015; Wakeford et al. 2017; Kilpatrick et al. 2018; Wakeford et al. 2018).

In addition, observational campaigns using ground-based telescopes at low resolution are expanding the number of giant planets with atmospheric characterization for example surveys using the *Very Large Telescope* (VLT) FOCAL Reducer and Spectrograph (FORSS2) (e.g., Bean et al. 2010; Nikolov et al. 2016; Gibson et al. 2017; Nikolov et al. 2018; Carter et al. 2020), the Arizona-CfA-Católica Exoplanet Spectroscopy Survey (ACCESS) (e.g., Rackham et al. 2017; Bixel et al. 2019; Espinoza et al. 2019b; McGruder et al. 2020; Kirk et al. 2021; Weaver et al. 2020, 2021; Allen et al. 2022; McGruder et al. 2022, 2023) and The Low Resolution Ground-Based Exoplanet Atmosphere Survey using Transmission Spectroscopy (LRG-BEASTS) (e.g., Kirk et al. 2018, 2019; Alderson et al. 2020; Kirk et al. 2021; Ahrer et al. 2022, 2023).

Most of the results mentioned above correspond to atmospheric observations of Jupiter to Saturn-sized planets; however, some involve smaller, Neptune-sized planets that have yielded interesting findings (e.g., HAT-P-11b: Deming et al. 2011; Fraine et al. 2014; Huber et al. 2017; GJ-436b: Ehrenreich et al. 2015; Bourrier et al. 2016; HAT-P-26b: Stevenson et al. 2016; Wakeford et al. 2017; MacDonald & Madhusudhan 2019).

Transmission spectra in optical and near-ultraviolet (NUV) wavelengths are particularly important because they enable studies of condensation clouds and photochemical hazes in the atmospheres of exoplanets. Physical processes like Rayleigh or Mie scattering produced by aerosols result in a continuum slope at these short wavelengths which can be used to understand the cloud composition and constrain haze properties (Wakeford et al. 2017a; Alam et al. 2020; Wong et al. 2020). Clouds and hazes are critical elements of planetary atmospheres, playing a pivotal role in controlling radiative processes such as transmission, reflection, and emission (Gao et al. 2021). In the context of transmission, clouds can absorb light which increases the opacity of the atmosphere at high altitudes preventing measurements deeper down in the atmosphere, significantly limiting our ability to accurately interpret exoplanet spectra. This effect is particularly notable in the water vapor (H_2O) feature at $\sim 1.4 \mu\text{m}$ (e.g., Sing et al. 2016). The combination of observations in the optical and near-infrared can provide insights into a planet’s metallicity through H_2O abundances and offer constraints on the opacity of clouds if they are present (Gao et al. 2020). Constraining H_2O provides essential clues for identifying planet formation scenarios (e.g., Öberg et al. 2011; Mordasini et al. 2016).

In the Solar System, the metallicity of giant planets is measured using CH_4 abundances and is expressed as the ratio C/H. For the gas giants, Jupiter and Saturn, C/H is $\sim 4\times$ solar and $\sim 10\times$ solar, respectively (Atreya et al. 2016). In the case of the ice giants, Neptune and Uranus, they are $\sim 80\times$ solar (Karkoschka & Tomasko 2011; Sromovsky et al. 2011). This trend is consistent with the core accretion model of planet formation (Pollack et al. 1996). For exoplanets, water absorption features have been widely used as a proxy for metallicity measurements (e.g., Kreidberg et al. 2014b; Fraine et al. 2014; Wakeford et al. 2018), expressed as the ratio O/H. However, studies of exoplanets with lower masses, including Neptune-like planets and super-Earths have shown to be challenging to constrain. Fraine et al. (2014) reported the first detection of H_2O in the exo-Neptune HAT-P-11b with a derived metallicity ranging from 1 to $700\times$ solar; thereafter, Wakeford et al. (2017) published a well-constrained metallicity for HAT-P-26b with an uncertainty of slightly more than one order of magnitude. HST’s coverage in the blue-optical wavelength range can help to disentangle the degeneracy between clouds and the water feature, providing constraints for clouds and metallicity measurements (Fairman et al. 2024).

The focus of this study is the warm Neptune-sized exoplanet HAT-P-26b discovered in 2011 (Hartman et al. 2011). This planet lies in a 4.23 day orbit with $R_p = 6.33 R_\oplus$ and $M_p = 18.6 M_\oplus$ and a low gravity $\log g_p = 2.65 \text{ cm s}^{-2}$. The low gravity in combination with the planet’s temperature ($T_{\text{eq}} = 1001 \text{ K}$) contributes to a large atmospheric scale height ($\sim 804 \text{ km}$), making it favorable for characterization studies using transmission spectroscopy. HAT-P-26b has been widely studied through different facilities, first using the Spitzer Space Telescope (Fazio et al. 2004), from ground-based telescopes (Stevenson et al. 2016; Vissapragada et al. 2022; A-thano et al. 2023), with HST (Wakeford et al. 2017) and analytically (MacDonald & Madhusudhan 2019). This target is the first exo-Neptune with a well-constrained metallicity, $\text{O}/\text{H} = 4.8_{-4.0}^{+21.5} \times$ solar. Wakeford et al. (2017) found that the metallicity of this planet falls below the trend in mass-metallicity observed in giant planets from the Solar System, and smaller than what is expected for a planet with its mass from core-accretion scenarios (Fortney et al. 2013). Furthermore, MacDonald & Madhusudhan (2019) did a comprehensive atmospheric retrieval analysis, making use of all available observations, to understand the atmospheric properties of HAT-P-26b. They report an updated value of metallicity $\text{O}/\text{H} = 18.1_{-11.3}^{+25.9} \times$ solar, suggesting a formation scenario with planetesimal accretion, which is still below that of Neptune. These results raise ques-

tions about HAT-P-26b’s formation and evolution process. Motivated by these studies, we add a new optical transmission spectrum to all the previous observations of this planet and provide an extended transmission spectrum from the optical to infrared with a retrieval analysis of its atmospheric properties.

In this paper, we present a new optical transmission spectrum of the warm Neptune HAT-P-26b, observed as part of the HST Panchromatic Comparative Exoplanet Treasury (PanCET) program (GO-14767, PIs: D. Sing and M. López-Morales). The scientific objectives of PanCET are to deliver a consistent and statistically significant comparative study of 20 exoplanet atmospheres, focusing on clouds, hazes, and chemical compositions across the ultraviolet (UV), optical and infrared (IR) wavelengths. This program provides unique observations in the UV and blue-optical wavelengths which are not accessible with the *James Webb Space Telescope* (JWST). The analysis of this project was carried out in conjunction with the Sculpting Hubble’s Exoplanet Legacy (SHEL) program (HST GO-16634, PI: D. Sing). Where the goals of the program are to analyze all HST archival observations of transiting exoplanets using a uniform and homogeneous reduction technique. The structure of this paper is as follows: [Section 2](#) describes the observations and data reduction process, [Section 3](#) details the systematics detrending and analysis of the transit light curves, in [Section 4](#) we present the results along with a discussion of them in [Section 5](#) and present the conclusions in [Section 6](#).

2. OBSERVATIONS AND DATA REDUCTION

2.1. Observations

We observed two transits of HAT-P-26b as part of the HST PanCET program, both taken with the Space Telescope Imaging Spectrograph (STIS) G430L grating. Each transit was observed in a single visit during 2018 March 27 (visit 14) and 2019 June 14 (visit 13). The G430L grating covers the wavelength region from 2892 Å to 5700 Å, providing a low-resolution of $R = \lambda/\Delta\lambda = 500$. The visits were planned to include the transit event in the third orbit, ensuring sufficient out-of-transit baseline flux and good coverage between the second and third contact. HST orbits the Earth every ~ 96 minutes, with data collection halted during each orbit when HST is occulted by the Earth. This approach yielded five consecutive orbits, resulting in a total of 48 spectra per visit per instrument. Of these, we used 43, discarding the first exposure of each HST orbit, as it has historically shown lower fluxes than the subsequent exposures ([Brown et al. 2001](#); [Sing et al. 2011, 2019](#)). Each spectrum had an exposure time of 253 seconds, they were taken with the

Table 1. Stellar and Planetary Parameters of the HAT-P-26 system.

Stellar Parameters	Value	Ref.
Radius	$0.788_{-0.043}^{+0.098} R_{\odot}$	[1]
Mass	$0.816 \pm 0.033 M_{\odot}$	[1]
Density (ρ_*)	$1774 \pm 108 \text{ kg/m}^3$	[3]
Eff. temperature (T_{eff})	$5011 \pm 55 \text{ K}$	[2]
Planetary Parameters	Value	Ref.
Radius	$0.565_{-0.032}^{+0.072} R_J$	[1]
Mass	$0.059 \pm 0.007 M_J$	[1]
Orbital period (P)	$4.234516 \pm 0.000015 \text{ days}$	[1]
Scaled semi-major axis (a/R_*)	11.89 ± 0.417	[3]
Transit center time (T_0)	$2456901.059458 \text{ BJD}$	[4]
Impact parameter (b)	0.395 ± 0.116	[3]
Eccentricity (e)	0.124 ± 0.060	[1]
Inclination (i)	$88.09 \pm 0.553 \text{ deg}$	[3]
Surface gravity ($\log g_p$)	$2.65_{-0.10}^{+0.08} \text{ cm/s}^2$	[1]
Argument of periastron (ω)	$54 \pm 165 \text{ deg}$	[1]
Eq. Temperature (T_{eq})	$1001_{-37}^{+66} \text{ K}$	[1]
Distance (a)	$0.0479 \pm 0.0006 \text{ AU}$	[1]

[1] [Hartman et al. \(2011\)](#)

[2] [Mortier et al. \(2013\)](#)

[3] [Wakeford et al. \(2017\)](#)

[4] this work

$52 \times 2 \text{ arcsec}^2$ slit to minimize slit losses, and using a reduced sub-array of 1024×128 pixels to reduce readout times.

2.2. Data Reduction

We reduced the STIS G430L spectra following the methodology described in [Allen et al. \(2024\)](#), which utilizes the pipeline from the SHEL program. This approach is briefly summarized here. We start with the flat-fielded products from MAST (`*flt.fits`) as well as the engineering jitter files (`*jit.fits`) and extract the respective time-series exposures. At this stage, we start the data cleaning processes. Initially, we use the cleaning function to identify pixels with a poor data quality flag in STIS. Subsequently, we use the technique called difference images to remove cosmic rays as described in [Nikolov et al. \(2014\)](#), which appear as an excess in flux. The next step is to find and correct for hot and cold pixels, that will not be detected using in the previous steps, using a spline-fitting method. Lastly, implementing the same spline-fitting technique, we further investigate any potentially faulty pixels that may have been overlooked. Once we have our data cleaned, we proceed with the spectral extraction method using two different techniques. We use optimal extraction ([Marsh](#)

1989) as implemented in Brahm et al. (2017). This approach uses a series of polynomials to model the spectral profile. The method assigns a weight to each pixel in the science frame, facilitating a weighted extraction of the spectrum. We apply an aperture size of 15 pixels and we compare it to the “classical” method of a spectral extraction which uses a box with a 13-pixel aperture width around the central trace (Huitson et al. 2013; Sing et al. 2013; Wakeford et al. 2017). We chose to proceed with the optimal extraction method as no significant differences were observed between the resulting spectra and the optimal extraction was strongly justified in Allen et al. (2024). For more details of each step in the data reduction process, see Allen et al. (2024). To ensure consistent analysis across the spectrum, a goal of the SHEL program, we reanalyze the STIS G750L observations presented in Wakeford et al. (2017) implementing the same analysis approach detailed above.

3. ANALYSIS

3.1. Systematics Detrending

Time-series observations taken with HST STIS are highly affected by instrument-related systematics. The main effect is due to the well-known thermal breathing of HST, a process in which the telescope warms up and cools down during its orbital cycle. This in turn causes the point-spread function (PSF) to change periodically and produces photometric changes in the light curves (Brown et al. 2001) which are correlated to HST’s orbital phase. These systematic errors in the spectrophotometry have limited the precision achieved. To model the systematics, we follow a procedure similar to Sing et al. (2011, 2019) and as implemented in the SHEL pipeline as described in Allen et al. (2024).

We utilize six jitter vectors that demonstrated the strongest correlation with the data: $V2_roll$, $V3_roll$, RA , DEC , $Latitude$ and $Longitude$. We also include three detrending parameters related to the spectral trace movement, one being the start of the trace in the y -value and two coefficients coming from the trace fitting. Lastly, we include a fourth order polynomial of HST’s orbital phase. To decorrelate these detrending vectors, we first normalize each measured quantity by subtracting the mean value and then dividing by the standard deviation.

We use a Gaussian process (GP) model over a linear model to handle the systematics as it was concluded in Allen et al. (2024), where the choice of detrending method does not significantly impact the transmission spectrum’s shape although it affects the uncertainties. To prevent overfitting, we apply an exponential prior to the GP detrending vector coefficients which heavily

penalizes unfavorable regressors. Starting with the 10 jitter vectors mentioned before, we perform principal component analysis (PCA) to generate a set of vectors that are not correlated with each other. We use them as an initial set of input parameters aiming to reduce the dimensionality of the fit with the expectation of the exponential priors. First, we re-normalize the principal components (PCs) and test the GP detrending method with the PCs ranging from 1 to 10 as input vectors. Upon completion of testing, we found that the optimal systematics model for the G430L and G750L data is eight PCs. Implementing the best systematics model, we perform a white light curve fit as seen in Figure 1 and spectroscopic fits in Figure 2 and Figure 3.

3.2. White Light Curve Fitting

After extracting the spectra and cleaning it, we start the analysis of the time-series light curves. To obtain a white light curve, we sum the flux over the entire wavelength range, from 0.29 to 0.57 μm for G430L and from 0.53 to 1.02 μm for G750L, for each exposure. We convert the exposure time stamps given in JD_{UTC} to BJD_{TBD} using *barycorrpy* (Kanodia & Wright 2018). We normalize each white light curve with respect to the median flux value of the out of transit data in a visit, and for the light curve fits we use *juliet* (Espinoza et al. 2019a). The modeled flux measurement consisted of a combination of a geometric transit model with limb darkening, and a systematic error correction model, the latter described in Section 3.1. In this study, we adopt the stellar and planetary parameters from Hartman et al. (2011), as several parameters in Wakeford et al. (2017) are derived from Hartman et al. (2011). For the remaining parameters not included in Hartman et al. (2011), we directly use those from Wakeford et al. (2017). This approach ensures consistency and allows for a meaningful comparison with the findings of Wakeford et al. (2017) (see Table 1). We used an exponential prior for the detrending vectors with the standard values from the SHEL pipeline. In the case of a resulting poor fit to the data, we tested using a range of exponential priors, a range of priors for the σ_w (a jitter added in quadrature to the error bars of the instrument) and GP_sigma (amplitude of the GP) parameters to improve the fits which was accomplished without affecting the resulting R_p/R_s and its error. During the transit fit, we fix all of the system parameters except R_p/R_s , we fit for all the coefficients of the systematics detrending vectors and additionally fit for $mflux$ (the offset relative flux for the photometric instrument) and σ_w which are inherent parameters from *juliet*. When dealing with limb darkening, we fix the values to the calculation from

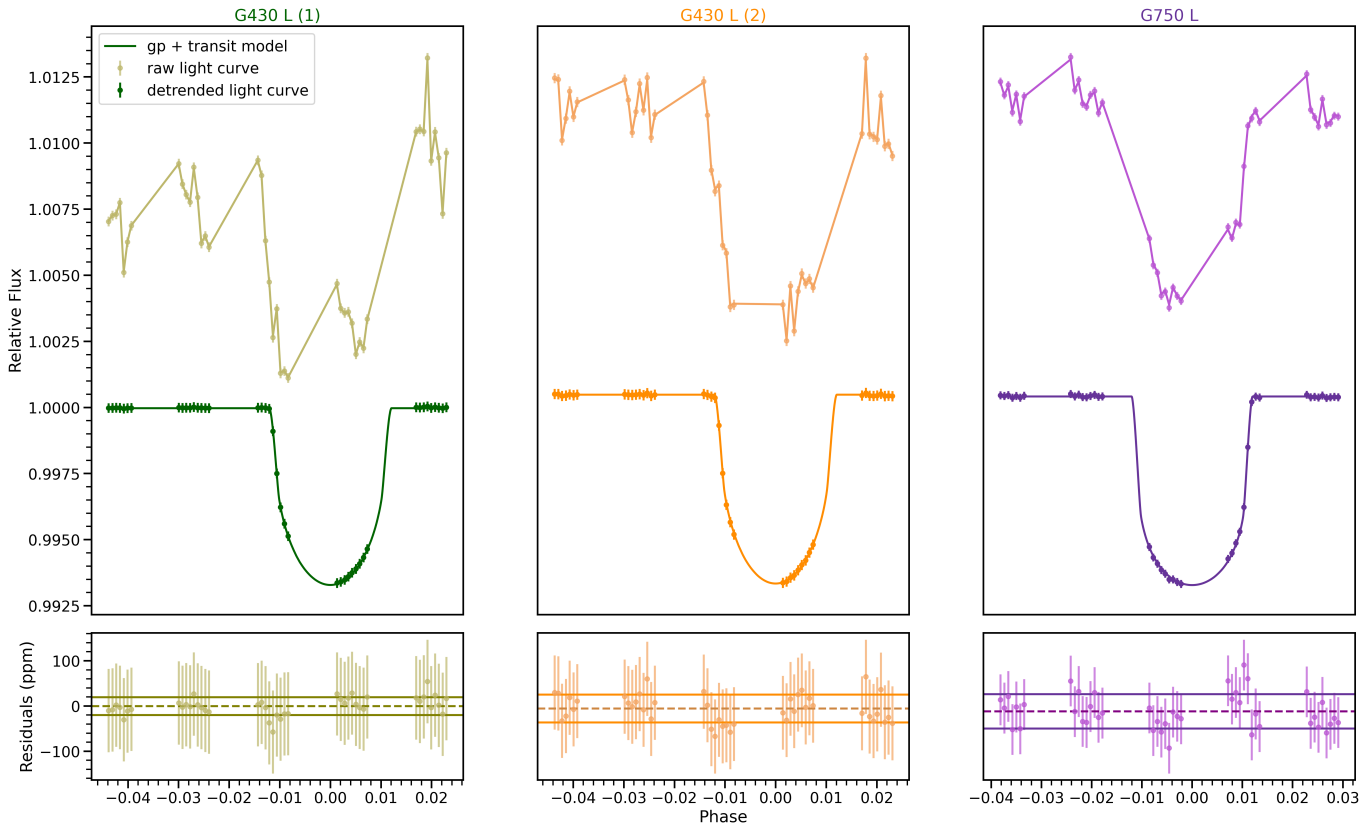


Figure 1. *Top:* The raw and detrended white light curves for each HST visit in the STIS G430L (green and orange) and STIS G750L gratings (purple). The best-fit light curve model is overplotted. *Bottom:* Corresponding residuals from the white light curve fit are shown in the colored circles. The solid lines correspond to one times the standard deviation.

the theory using *ExoTiC-LD* (Grant & Wakeford 2024) where we use the Kurucz stellar grid (Kurucz 1993), we assume $T_{eff} = 5079 \pm 88$, $[M/H] = -0.04 \pm 0.08$ and $\log g_{\star} = 4.56 \pm 0.06$ (Hartman et al. 2011) and use the quadratic limb darkening law parametrization from Kipping of q_1 and q_2 (Kipping 2013). The SHEL pipeline has several options for the nested sampling under which we select *dynamic dynesty* for the posterior sampling of the parameter errors.

3.3. Spectral Light Curve Fitting

To produce spectroscopic light curves for the G430L observations, we bin the data into four spectrophotometric channels between $0.29 - 0.57 \mu\text{m}$. The binning scheme was determined by balancing signal-to-noise ratio (SNR) and spectral resolution, notably the spectra in the bluer end have lower counts than in the redder part. As a result, the SNR across bins ranges from approximately 17,000 to 48,000 for both visits. We use continuous binning to avoid stellar absorption lines; by carefully selecting bin widths to avoid known stellar lines, the method reduces systematic noise and improves SNR. Proper binning strategies enhance the reliability of spectral analysis by minimizing stellar interference. This ap-

proach is essential for accurately retrieving exoplanet atmospheric properties, particularly in cases where stellar absorption lines overlap with planetary features. Using the results and testing from the white light curve fit, we carry out the same fits for the spectroscopic light curves where we fix the system parameters minus R_p/R_s , fit for the coefficients of the systematics detrending vectors and additionally fit for $mflux$ and $sigma_w$. For limb darkening, we calculate the coefficients using *ExoTiC-LD* for each bin and fix the values.

In the case of G750L, we used a similar bin configuration as Wakeford et al. (2017) as we wanted to achieve a consistent reduction to compare with the previous published results. We thus binned the G750L spectra into seven spectral bands between $0.53 - 1.02 \mu\text{m}$. Following that, we performed the same fitting approach as for the G430L observations discussed above.

4. RESULTS

The results of our white light curve analysis of HAT-P-26b are listed in Table 2. The raw, systematics-corrected light curves and the best-fit transit models are shown in Figure 1. We note that when comparing the two transit depths from the two STIS G430L visits, the values

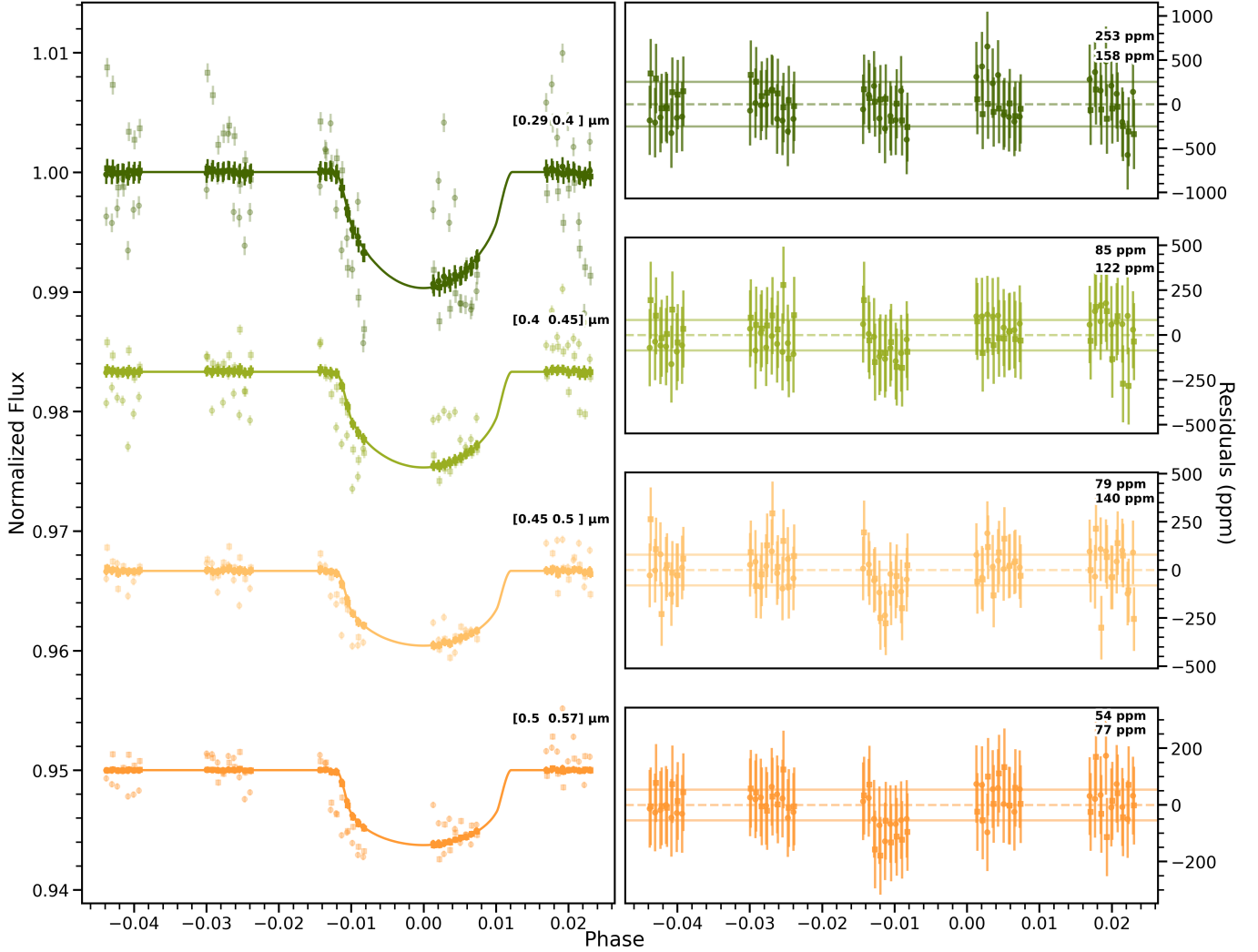


Figure 2. Spectroscopic light curve fits for HST STIS G430L (visit 13 and visit 14, phased together). Left panel: Detrended light curves (darker points), raw data from visit 13 (circles) and visit 14 (squares), and the best-fit transit model (solid lines). Each wavelength bin is offset vertically by an arbitrary constant for clarity and the binning wavelength range is shown above the post-transit baseline. Right panel: Corresponding residuals in parts per million (ppm). The standard deviation of the residuals is reported in the residuals plot, we report two values which correspond to the two different visits.

mostly agree with each other to within 1.5σ , indicating that there is not significant stellar photometric variability between the visits and HAT-P-26 is considered to be a quiet star (Wakeford et al. 2017).

Table 2. White Light Curve Derived Radii

Instrument	Wavelength (μm)	R_p/R_s
STIS G430L (1)	0.29 – 0.57	$0.0679^{+0.0048}_{-0.0042}$
STIS G430L (2)	0.29 – 0.57	$0.0758^{+0.0022}_{-0.0022}$
STIS G750L	0.53 – 1.02	$0.0700^{+0.0015}_{-0.0017}$

We compare our re-analyzed transmission spectrum of HAT-P-26b using HST G750L with the previously published observations in Wakeford et al. (2017) in Figure 4.

We can see that there is an agreement between the two reductions with the exception of one data point in the region between $0.8 - 0.9 \mu\text{m}$. The discrepancies likely arise because the pipeline used in this analysis implements GPs while the published one uses a Lavenberg-Marquart (L-M) least-squares algorithm.

We construct an extended transmission spectrum for HAT-P-26b covering from the optical to infrared, $0.29 - 5.0 \mu\text{m}$, by combining STIS, WFC3 and Spitzer observations where the WFC3 and Spitzer points come from Wakeford et al. (2017). Table 3 shows the measured planet-star radius ratios from the spectroscopic light curves analysis with the bin configuration for each grating. For the case of G430L, we use a joint fit function that takes into account the two corresponding visits

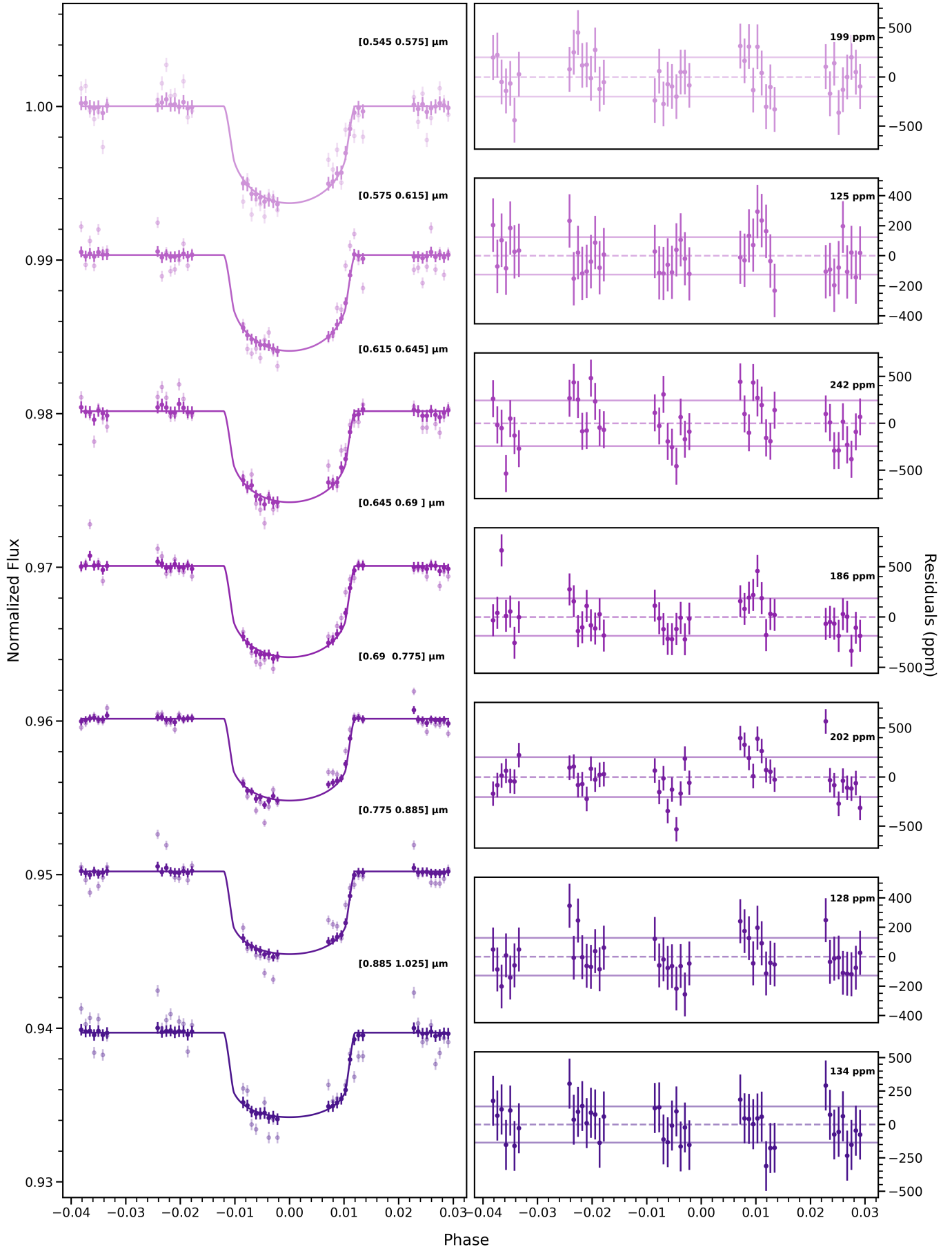


Figure 3. Same as Figure 2, but for one visit with the G750L grating.

Table 3. Spectroscopic Light Curve Fit Results

Wavelength (μm)	R_p/R_s
STIS G430L	
0.29 – 0.40	0.0844 ± 0.0057
0.40 – 0.45	0.0780 ± 0.0027
0.45 – 0.50	0.0700 ± 0.0017
0.50 – 0.57	0.0707 ± 0.0021
STIS G750L	
0.53 – 0.58	0.0716 ± 0.0024
0.58 – 0.62	0.0713 ± 0.0025
0.62 – 0.65	0.0699 ± 0.0020
0.65 – 0.69	0.0706 ± 0.0016
0.69 – 0.78	0.0671 ± 0.0015
0.78 – 0.89	0.0681 ± 0.0021
0.90 – 1.02	0.0694 ± 0.0027

and outputs a combined R_p/R_s with its respective error. With multiple visits, *juliet* assumes that the system parameters are the same across both visits and only one posterior distribution is assumed for R_p/R_s . This parameter is generated based on the combined data and the errors are given by the standard deviation of the posterior distribution.

The transmission spectrum is shown in Figure 5 in comparison with a retrieval atmospheric model (to be detailed in Section 4.1). A compilation of the spectroscopic light curve channels with the corresponding best-fit transit models is provided in Figure 2 and Figure 3. Looking at Figure 5, we see that the transmission spectrum shows a moderate slope in the blue optical, suggesting Rayleigh-like scattering from aerosols.

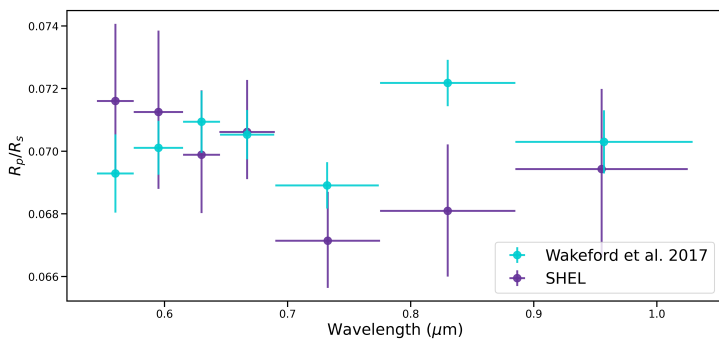


Figure 4. Transmission spectrum comparison of HAT-P-26b from HST STIS G750L grating. The data points shown in purple correspond to the work done here and the ones in light blue to the analysis from Wakeford et al. (2017).

4.1. Atmospheric Retrieval: ATMO

To investigate the atmospheric properties of HAT-P-26b, we used the 1-D radiative-convective equilib-

rium model ATMO (Tremblin et al. 2015, 2016; Goyal et al. 2018) which has been widely used as a spectroscopic retrieval model for planetary atmospheres in both transmission and emission spectroscopy (Wakeford et al. 2017; Evans et al. 2017; Alam et al. 2018; Rathcke et al. 2021; Fu et al. 2022). With the new STIS data, we focused our model comparisons on differing cloud properties. We do not test other parameters as there is a clear lack of Na or K absorption features in the measured spectrum (Fairman et al. 2024). For the chemistry, we use a free-element chemical equilibrium approach where we let C and O (C/C_\odot and O/O_\odot) to be free with the remaining elements to be varied with a single trace metallicity parameter (Z_{tr}/Z_\odot). In our spectrum, water is the only prevalent molecular feature making O/O_\odot the best constraining parameter. For this scenario, oxygen is a proxy for the metallicity of the planet.

The ATMO retrieval model incorporates a relatively straightforward approach to modeling clouds and hazes, and does not account for the distribution of aerosol particles (Goyal et al. 2018). The scattering from aerosol “haze” is represented as enhanced Rayleigh-like scattering. For the condensate “cloud” absorption, it is assumed to exhibit a gray wavelength dependence. ATMO implements an aerosol “haze” scattering with δ_{haze} , an empirical enhancement factor, the scattering cross section of molecular hydrogen at $0.35 \mu\text{m}$ (σ_0) and a factor that determines the wavelength dependence (α_{haze}). For the “cloud” absorption, it uses an empirical value for the strength of the gray scattering (δ_{cloud}) and the scattering opacity due to molecular hydrogen at $0.35 \mu\text{m}$ (κ_{H_2}). These parameters and their bounds help describe the effects of clouds and hazes in the atmospheric model implemented in the retrieval. To fit the data we consider four different atmospheric retrieval models: clouds + hazes, clouds only, hazes only and no clouds or hazes. For each case, we assumed an isothermal temperature structure based on the conclusions in Wakeford et al. (2017) and we fit for temperature, planetary radius, cloud and haze opacity (depending on the case) and for the abundances of H_2O (Barber et al. 2006), CO_2 (Tashkun & Perevalov 2011), CO (Rothman et al. 2010), CH_4 (Yurchenko & Tennyson 2014), NH_3 (Yurchenko et al. 2011), H_2S (Rothman et al. 2013), HCN , C_2H_2 and SO_2 (Underwood et al. 2016)(see Goyal et al. (2018, 2020) for full description).

The results of our ATMO retrieval fits are shown in Table 4. To determine relevant parameters such as metallicity, temperature, C/O ratio and α_{haze} , we employ Bayesian Model Averaging (BMA) by combining the posterior distributions of all models, with each model’s contribution weighted according to its Bayesian

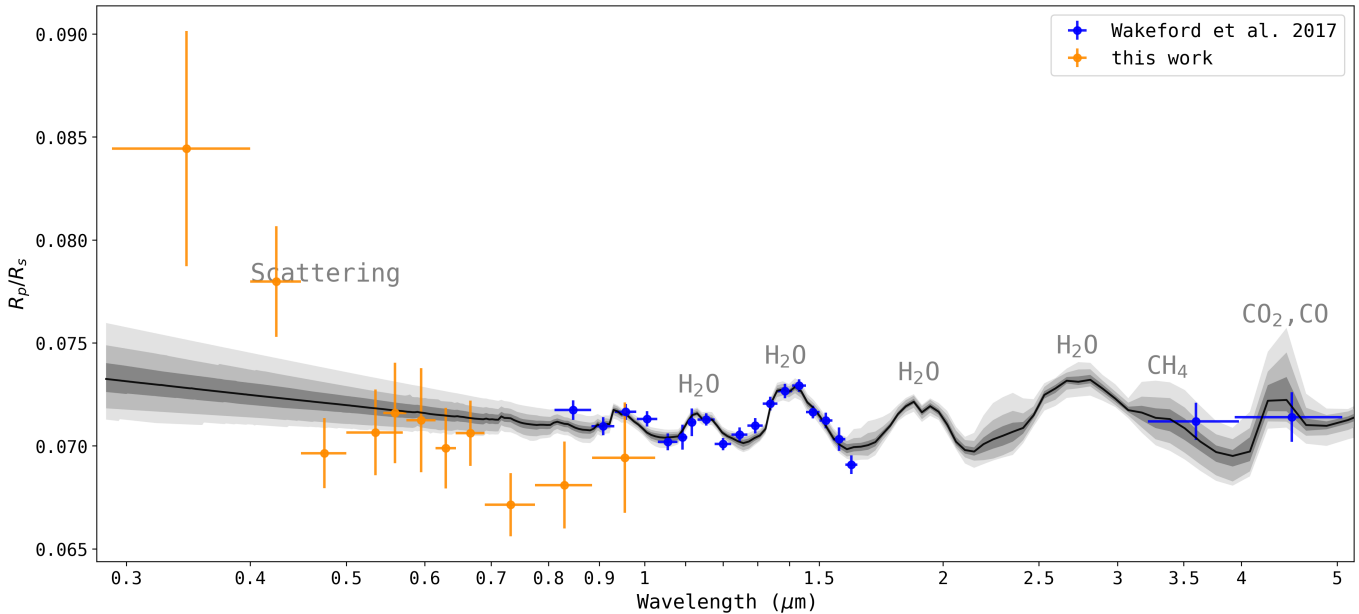


Figure 5. Broadband transmission spectrum of HAT-P-26b from HST STIS + WFC3 + Spitzer IRAC with the best-fitting model (black line) derived using the retrieval code ATMO. The work presented here is colored in orange using STIS G430L and G750L while the data from Wakeford et al. (2017) is shown in blue corresponding to WFC3 G102 and G141, and Spitzer IRAC. The best-fitting model is cloud-free and includes haze opacity. We show the results for model with hazes only with 1σ , 2σ and 3σ uncertainty in the dark to light gray shaded regions.

evidence following Wakeford et al. (2016); Wakeford et al. (2017). The Bayesian evidence for a given model (E_q) is linked to the Bayesian Information Criterion (BIC) through an approximation of the marginal likelihood, expressed as

$$\ln E_q = \ln P(D|S_q) \approx -\frac{1}{2}BIC \quad (1)$$

To compare different retrieval models, the evidence values are converted into weights (W_q) which represent the relative probability of each model. These weights are determined by normalizing the evidence values across all models as

$$W_q = \frac{E_q}{\sum_{q=0}^{N_q} E_q} \quad (2)$$

The weighted mean (α_m) of a parameter (α_q) is computed using these weights to account for contributions from different models

$$\alpha_m = \sum_{q=0}^{N_q} (W_q \times \alpha_q) \quad (3)$$

The overall uncertainty, $\sigma(\alpha)$,

$$\sigma(\alpha) = \sqrt{\sum_{q=0}^{N_q} W_q [(\alpha_q - \alpha_m)^2 + \sigma_{\alpha_q}^2]} \quad (4)$$

incorporates both the variance of individual parameter values around the mean and their associated uncertainties. This approach ensures that the final uncertainty reflects both the spread of parameter estimates and the confidence in each model's contribution. Our retrieval analysis finds a 15_{-8}^{+22} solar metallicity. The retrieved slope parameter (α_{haze}) exhibits a small increase when clouds are included in the model. However, given the propagated uncertainties, this difference is not statistically significant. The confidence interval overlap indicates that the slopes from both models are consistent within error. Consequently, we find no strong evidence that the inclusion of clouds significantly alters the retrieved haze slope for this exoplanet. The corner plot in Figure 6 shows the distributions of each parameter of interest.

5. DISCUSSION

We interpret the optical to infrared transmission spectrum of HAT-P-26b in the context of the observed mass-metallicity relationship in exoplanetary atmospheres. Our retrieval of the 0.29 – 5.0 μm HST + Spitzer spectrum indicates the presence of a scattering slope and water vapor (H_2O), the latter initially reported in Wakeford et al. (2017). With our new wavelength coverage in the blue optical we explored previous predictions of an absorbing cloud deck (Wakeford et al. (2017)) which we do not find but rather a scattering

Table 4. Atmospheric retrieval configuration scenarios with their respective results.

Model	Hazes Only	Clouds + Hazes	Clouds Only	No Clouds/Hazes	BMA
χ^2	40.16	40.58	51.80	75.46	
χ^2_ν	1.67	1.76	2.07	2.90	
BIC	62.41	68.05	71.11	91.74	
W_q	0.93	0.056	0.012	2.0×10^{-8}	
Temperature (K)	714^{+85}_{-49}	730^{+76}_{-73}	703^{+72}_{-62}	896^{+84}_{-51}	715^{+84}_{-51}
$\log[(Z_{tr}/Z_\odot)]$	$-0.75^{+2.49}_{-2.27}$	$-1.17^{+2.43}_{-2.19}$	$-0.05^{+2.57}_{-2.58}$	$-0.53^{+3.15}_{-3.45}$	$-0.76^{+2.49}_{-2.27}$
R_{pl} (Jup)	$0.5587^{+0.0047}_{-0.0050}$	$0.5589^{+0.0050}_{-0.0049}$	$0.5555^{+0.0057}_{-0.0052}$	$0.5530^{+0.0012}_{-0.0014}$	$0.5600^{+0.0047}_{-0.0050}$
α_{haze}	$2.3^{+0.8}_{-0.6}$	$2.5^{+0.7}_{-0.7}$	—	—	$2.3^{+0.8}_{-0.6}$
$\log[(O/O_\odot)]$	$1.2^{+0.4}_{-0.3}$	$1.1^{+0.4}_{-0.5}$	$1.2^{+0.4}_{-0.3}$	$2.5^{+0.1}_{-0.1}$	$1.2^{+0.4}_{-0.3}$
O/O_\odot (\times solar)	14^{+22}_{-8}	13^{+17}_{-9}	17^{+23}_{-9}	288^{+115}_{-70}	15^{+22}_{-8}
C/O	$0.004^{+0.020}_{-0.003}$	$0.005^{+0.003}_{-0.003}$	$0.003^{+0.006}_{-0.002}$	$0.0004^{+0.0060}_{-0.0004}$	$0.004^{+0.020}_{-0.003}$
P_{cloud} (mbar)	—	$0.48^{+0.07}_{-0.07}$	$0.24^{+0.07}_{-0.07}$	—	$0.44^{+0.12}_{-0.12}$

Note: The number of data points (N) used were 31 for all cases. For the number of parameters (k), we used 8, 6, 7, and 5, listed in the same order as the models in the table. The degrees of freedom (DOF) for each model were 24, 23, 25, and 26, following the same order.

slope best explained by haze-dominated scenario. Considering the haze properties, we find that the scattering alpha ($\alpha_{haze} = 2.3^{+0.8}_{-0.6}$) indicates a weaker wavelength-dependence than Rayleigh scattering ($\alpha_{haze} = 4$) which suggests absorbing rather than purely scattering particles, this can be caused by larger particles, specific particle compositions or a mix of particle sizes such as from settling grains (Pont et al. 2013).

An essential objective of exoplanet atmospheric studies is to connect atmospheric properties to planet formation history, to better understand the evolution of close-in giant planets from their formation to current day locations and the impact of growth and migration on their atmospheric properties. Metallicity measurements provide a crucial link to planet formation mechanisms. With the metallicity derived using ATMO ($15^{+22}_{-8} \times$ solar) we observe that HAT-P-26b lies below the expected mass-metallicity trend for exoplanets when compared to our Solar System’s gas giants ($\sim 80 \pm 20 \times$ solar for Neptune), placing it $\sim 3\sigma$ below the trend. If we compare our result with what was previously derived in Wakeford et al. (2017) ($4.8^{+21.5}_{-4.0} \times$ solar) and MacDonald & Madhusudhan (2019) ($18.1^{+25.9}_{-11.3} \times$ solar), our result is in agreement to $< 1\sigma$ for both cases. The overall conclusion from our result is consistent with the previous findings described in Wakeford et al. (2017), where its formation scenario is aligned with envelope accretion models (Lee & Chiang 2016). This scenario argues that the

majority of hot Neptunes acquire their envelopes in situ, just before their protoplanetary disks disappear.

We note that the addition of the optical wavelength covered by the STIS G430L grating helps provide constraints on the metallicity value and most importantly, insights and constraints on the aerosol properties (Sing et al. 2011; Pont et al. 2013; Rustamkulov et al. 2023; Fu et al. 2024; Fairman et al. 2024).

6. CONCLUSIONS

We presented new HST G430L (0.29 – 0.57 μ m) transmission spectra and a re-reduction of the HST STIS G750L (0.53 – 1.02 μ m) previously published data along with previous observations from HST WFC3 G102 and G141, and Spitzer of the warm Neptune HAT-P-26b. The main findings are summarized below:

1. The transmission spectrum of HAT-P-26b is characterized by an optical scattering slope that is less wavelength-dependent than Rayleigh scattering, indicating larger particles or a mix of particle sizes.
2. We retrieve the planet’s atmospheric properties using ATMO. The result for metallicity, $15^{+22}_{-8} \times$ solar, is in agreement with the previously published result of HAT-P-26b from Wakeford et al. (2017) and MacDonald & Madhusudhan (2019).

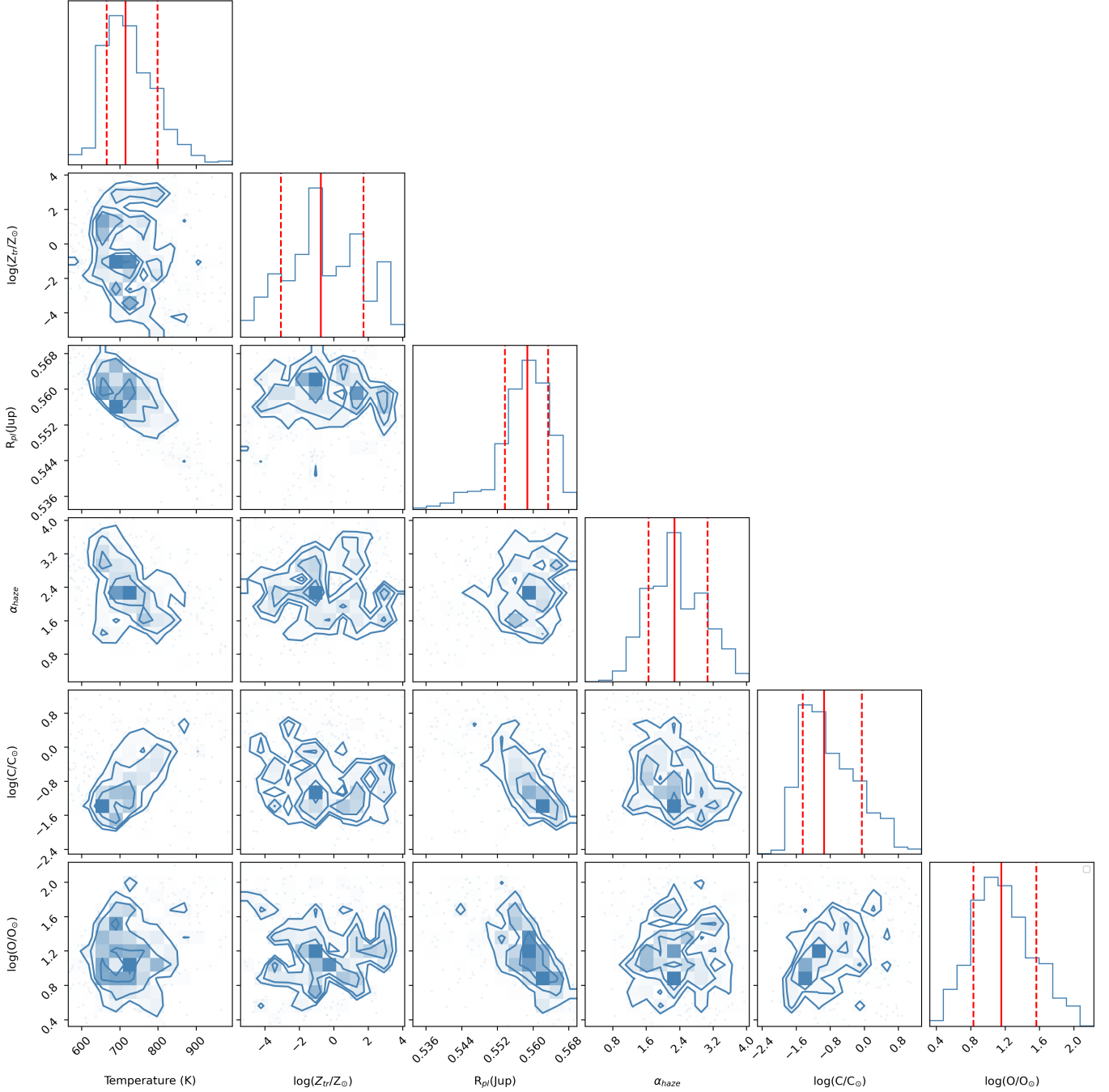


Figure 6. HAT-P-26b retrieval posterior showing the distribution of the retrieved parameters from the HST + Spitzer transmission spectrum using ATMO for the best-fitting model (haze-only scenario). Contours corresponding to 1, 1.5 and 2σ are shown (blue). The 1D histograms show the parameters’ mean value and 1σ range (red).

HAT-P-26b has been observed as part of the JWST Cycle 1 Guaranteed Time Observation (GTO) programs (GTO-1312, PI: N. Lewis) with multiple instruments (e.g., NIRISS SOSS and NIRSpec G395H) which will provide further constraints on the atmospheric composition and structure. Complementing the new JWST observations with the existing HAT-P-26b data includ-

ing the HST STIS G430L analysis presented here, significantly enhances the ability to characterize the planet’s atmosphere. The inclusion of STIS G430L extends the spectral coverage into the visible range, enabling improved constraints on optical scattering slopes and haze properties. This data serves as a critical baseline for interpreting molecular absorption characteristics observed

in the infrared by WFC3, Spitzer, and JWST, ensuring consistency and accuracy across the entire spectrum. By integrating these datasets, a more comprehensive and precise understanding of HAT-P-26b’s atmospheric properties and formation history can be achieved.

Software: astropy (Astropy Collaboration et al. 2013, 2018), ATMO (Tremblin et al. 2015, 2016; Goyal et al. 2018), barycorrpy (Kanodia & Wright 2018), batman (Kreidberg 2015), corner (Foreman-Mackey 2016), dynesty (Speagle 2020), george (Ambikasaran et al. 2015), juliet (Espinoza et al. 2019a), jupyter (Kluyver et al. 2016), matplotlib (Hunter 2007), multinest (Feroz & Hobson 2008; Feroz et al. 2009, 2019), NumPy (Haris et al. 2020), pandas (Pandas Development Team 2020;

Wes McKinney 2010), SciPy (Virtanen et al. 2020), transitspectroscopy (Espinoza 2022) .

ACKNOWLEDGMENTS

This work is based on observations made with the NASA/ ESA Hubble Space Telescope obtained at the Space Telescope Science Institute (STScI), which is operated by the Association of Universities for Research in Astronomy, Inc. The observations associated with this analysis are the HST-GO programs 14767 and 14110 and the datasets can be accessed via this DOI. Support for this work was provided by NASA through grants under the HST GO-14767 and HST AR-6634 program from STScI. The authors thank N. Espinoza for helpful discussions.

REFERENCES

- A-thano, N., Awiphan, S., Jiang, I.-G., et al. 2023, *AJ*, 166, 223, doi: [10.3847/1538-3881/acfeeaa](https://doi.org/10.3847/1538-3881/acfeeaa)
- Ahrer, E., Wheatley, P. J., Gandhi, S., et al. 2023, *MNRAS*, 521, 5636, doi: [10.1093/mnras/stad779](https://doi.org/10.1093/mnras/stad779)
- Ahrer, E., Wheatley, P. J., Kirk, J., et al. 2022, *MNRAS*, 510, 4857, doi: [10.1093/mnras/stab3805](https://doi.org/10.1093/mnras/stab3805)
- Alam, M. K., Nikolov, N., López-Morales, M., et al. 2018, *AJ*, 156, 298, doi: [10.3847/1538-3881/aace89](https://doi.org/10.3847/1538-3881/aace89)
- Alam, M. K., López-Morales, M., Nikolov, N., et al. 2020, *AJ*, 160, 51, doi: [10.3847/1538-3881/ab96cb](https://doi.org/10.3847/1538-3881/ab96cb)
- Alam, M. K., López-Morales, M., MacDonald, R. J., et al. 2021, *ApJL*, 906, L10, doi: [10.3847/2041-8213/abd18e](https://doi.org/10.3847/2041-8213/abd18e)
- Alderson, L., Kirk, J., López-Morales, M., et al. 2020, *MNRAS*, 497, 5182, doi: [10.1093/mnras/staa2315](https://doi.org/10.1093/mnras/staa2315)
- Allen, N. H., Espinoza, N., Jordán, A., et al. 2022, *AJ*, 164, 153, doi: [10.3847/1538-3881/ac8b74](https://doi.org/10.3847/1538-3881/ac8b74)
- Allen, N. H., Sing, D. K., Espinoza, N., et al. 2024, *The Astronomical Journal*, 168, 111, doi: [10.3847/1538-3881/ad58e1](https://doi.org/10.3847/1538-3881/ad58e1)
- Ambikasaran, S., Foreman-Mackey, D., Greengard, L., Hogg, D. W., & O’Neil, M. 2015, *IEEE Transactions on Pattern Analysis and Machine Intelligence*, 38, 252, doi: [10.1109/TPAMI.2015.2448083](https://doi.org/10.1109/TPAMI.2015.2448083)
- Astropy Collaboration, Robitaille, T. P., Tollerud, E. J., et al. 2013, *A&A*, 558, A33, doi: [10.1051/0004-6361/201322068](https://doi.org/10.1051/0004-6361/201322068)
- Astropy Collaboration, Price-Whelan, A. M., Sipőcz, B. M., et al. 2018, *AJ*, 156, 123, doi: [10.3847/1538-3881/aabc4f](https://doi.org/10.3847/1538-3881/aabc4f)
- Atreya, S. K., Crida, A., Guillot, T., et al. 2016, arXiv e-prints, arXiv:1606.04510, doi: [10.48550/arXiv.1606.04510](https://doi.org/10.48550/arXiv.1606.04510)
- Barber, R. J., Tennyson, J., Harris, G. J., & Tolchenov, R. N. 2006, *MNRAS*, 368, 1087, doi: [10.1111/j.1365-2966.2006.10184.x](https://doi.org/10.1111/j.1365-2966.2006.10184.x)
- Bean, J. L., Miller-Ricci Kempton, E., & Homeier, D. 2010, *Nature*, 468, 669, doi: [10.1038/nature09596](https://doi.org/10.1038/nature09596)
- Benneke, B., Knutson, H. A., Lothringer, J., et al. 2019, *Nature Astronomy*, 3, 813, doi: [10.1038/s41550-019-0800-5](https://doi.org/10.1038/s41550-019-0800-5)
- Bixel, A., Rackham, B. V., Apai, D., et al. 2019, *AJ*, 157, 68, doi: [10.3847/1538-3881/aaf9a3](https://doi.org/10.3847/1538-3881/aaf9a3)
- Bourrier, V., Lecavelier des Etangs, A., Ehrenreich, D., Tanaka, Y. A., & Vidotto, A. A. 2016, *A&A*, 591, A121, doi: [10.1051/0004-6361/201628362](https://doi.org/10.1051/0004-6361/201628362)
- Brahm, R., Jordán, A., & Espinoza, N. 2017, *PASP*, 129, 034002, doi: [10.1088/1538-3873/aa5455](https://doi.org/10.1088/1538-3873/aa5455)
- Brown, T. M., Charbonneau, D., Gilliland, R. L., Noyes, R. W., & Burrows, A. 2001, *ApJ*, 552, 699, doi: [10.1086/320580](https://doi.org/10.1086/320580)
- Carter, A. L., Nikolov, N., Sing, D. K., et al. 2020, *MNRAS*, 494, 5449, doi: [10.1093/mnras/staa1078](https://doi.org/10.1093/mnras/staa1078)
- Changeat, Q., Skinner, J. W., Cho, J. Y. K., et al. 2024, *ApJS*, 270, 34, doi: [10.3847/1538-4365/ad1191](https://doi.org/10.3847/1538-4365/ad1191)
- Charbonneau, D., Brown, T. M., Noyes, R. W., & Gilliland, R. L. 2002, *ApJ*, 568, 377, doi: [10.1086/338770](https://doi.org/10.1086/338770)
- Deming, D., Sada, P. V., Jackson, B., et al. 2011, *ApJ*, 740, 33, doi: [10.1088/0004-637X/740/1/33](https://doi.org/10.1088/0004-637X/740/1/33)
- Deming, D., Wilkins, A., McCullough, P., et al. 2013, *ApJ*, 774, 95, doi: [10.1088/0004-637X/774/2/95](https://doi.org/10.1088/0004-637X/774/2/95)
- Ehrenreich, D., Bourrier, V., Wheatley, P. J., et al. 2015, *Nature*, 522, 459, doi: [10.1038/nature14501](https://doi.org/10.1038/nature14501)
- Espinoza, N. 2022, *TransitSpectroscopy*, 0.3.11, Zenodo, doi: [10.5281/zenodo.6960924](https://doi.org/10.5281/zenodo.6960924)

- Espinoza, N., Kossakowski, D., & Brahm, R. 2019a, *MNRAS*, 490, 2262, doi: [10.1093/mnras/stz2688](https://doi.org/10.1093/mnras/stz2688)
- Espinoza, N., Rackham, B. V., Jordán, A., et al. 2019b, *MNRAS*, 482, 2065, doi: [10.1093/mnras/sty2691](https://doi.org/10.1093/mnras/sty2691)
- Evans, T. M., Sing, D. K., Kataria, T., et al. 2017, *Nature*, 548, 58, doi: [10.1038/nature23266](https://doi.org/10.1038/nature23266)
- Fairman, C., Wakeford, H. R., & MacDonald, R. J. 2024, *AJ*, 167, 240, doi: [10.3847/1538-3881/ad3454](https://doi.org/10.3847/1538-3881/ad3454)
- Fazio, G. G., Hora, J. L., Allen, L. E., et al. 2004, *ApJS*, 154, 10, doi: [10.1086/422843](https://doi.org/10.1086/422843)
- Feroz, F., & Hobson, M. P. 2008, *Monthly Notices of the Royal Astronomical Society*, 384, 449, doi: [10.1111/j.1365-2966.2007.12353.x](https://doi.org/10.1111/j.1365-2966.2007.12353.x)
- Feroz, F., Hobson, M. P., & Bridges, M. 2009, *Monthly Notices of the Royal Astronomical Society*, 398, 1601, doi: [10.1111/j.1365-2966.2009.14548.x](https://doi.org/10.1111/j.1365-2966.2009.14548.x)
- Feroz, F., Hobson, M. P., Cameron, E., & Pettitt, A. N. 2019, *The Open Journal of Astrophysics*, 2, 10, doi: [10.21105/astro.1306.2144](https://doi.org/10.21105/astro.1306.2144)
- Foreman-Mackey, D. 2016, *The Journal of Open Source Software*, 1, 24, doi: [10.21105/joss.00024](https://doi.org/10.21105/joss.00024)
- Fortney, J. J., Mordasini, C., Nettelmann, N., et al. 2013, *ApJ*, 775, 80, doi: [10.1088/0004-637X/775/1/80](https://doi.org/10.1088/0004-637X/775/1/80)
- Fraine, J., Deming, D., Benneke, B., et al. 2014, *Nature*, 513, 526, doi: [10.1038/nature13785](https://doi.org/10.1038/nature13785)
- Fu, G., Sing, D. K., Deming, D., et al. 2022, *AJ*, 163, 190, doi: [10.3847/1538-3881/ac58fc](https://doi.org/10.3847/1538-3881/ac58fc)
- Fu, G., Welbanks, L., Deming, D., et al. 2024, *arXiv e-prints*, arXiv:2407.06163, doi: [10.48550/arXiv.2407.06163](https://doi.org/10.48550/arXiv.2407.06163)
- Gao, P., Wakeford, H. R., Moran, S. E., & Parmentier, V. 2021, *Journal of Geophysical Research (Planets)*, 126, e06655, doi: [10.1029/2020JE006655](https://doi.org/10.1029/2020JE006655)
- Gao, P., Thorngren, D. P., Lee, E. K. H., et al. 2020, *Nature Astronomy*, 4, 951, doi: [10.1038/s41550-020-1114-3](https://doi.org/10.1038/s41550-020-1114-3)
- Gibson, N. P., Nikolov, N., Sing, D. K., et al. 2017, *MNRAS*, 467, 4591, doi: [10.1093/mnras/stx353](https://doi.org/10.1093/mnras/stx353)
- Goyal, J. M., Mayne, N., Sing, D. K., et al. 2018, *MNRAS*, 474, 5158, doi: [10.1093/mnras/stx3015](https://doi.org/10.1093/mnras/stx3015)
- Goyal, J. M., Mayne, N., Drummond, B., et al. 2020, *MNRAS*, 498, 4680, doi: [10.1093/mnras/staa2300](https://doi.org/10.1093/mnras/staa2300)
- Grant, D., & Wakeford, H. 2024, *The Journal of Open Source Software*, 9, 6816, doi: [10.21105/joss.06816](https://doi.org/10.21105/joss.06816)
- Harris, C. R., Millman, K. J., van der Walt, S. J., et al. 2020, *Nature*, 585, 357, doi: [10.1038/s41586-020-2649-2](https://doi.org/10.1038/s41586-020-2649-2)
- Hartman, J. D., Bakos, G. Á., Kipping, D. M., et al. 2011, *ApJ*, 728, 138, doi: [10.1088/0004-637X/728/2/138](https://doi.org/10.1088/0004-637X/728/2/138)
- Huber, K. F., Czesla, S., & Schmitt, J. H. M. M. 2017, *A&A*, 597, A113, doi: [10.1051/0004-6361/201629699](https://doi.org/10.1051/0004-6361/201629699)
- Huitson, C. M., Sing, D. K., Pont, F., et al. 2013, *MNRAS*, 434, 3252, doi: [10.1093/mnras/stt1243](https://doi.org/10.1093/mnras/stt1243)
- Hunter, J. D. 2007, *Computing in Science & Engineering*, 9, 90, doi: [10.1109/MCSE.2007.55](https://doi.org/10.1109/MCSE.2007.55)
- Kanodia, S., & Wright, J. 2018, *Research Notes of the American Astronomical Society*, 2, 4, doi: [10.3847/2515-5172/aaa4b7](https://doi.org/10.3847/2515-5172/aaa4b7)
- Karkoschka, E., & Tomasko, M. G. 2011, *Icarus*, 211, 780, doi: [10.1016/j.icarus.2010.08.013](https://doi.org/10.1016/j.icarus.2010.08.013)
- Kilpatrick, B. M., Cubillos, P. E., Stevenson, K. B., et al. 2018, *AJ*, 156, 103, doi: [10.3847/1538-3881/aacea7](https://doi.org/10.3847/1538-3881/aacea7)
- Kipping, D. M. 2013, *MNRAS*, 435, 2152, doi: [10.1093/mnras/stt1435](https://doi.org/10.1093/mnras/stt1435)
- Kirk, J., López-Morales, M., Wheatley, P. J., et al. 2019, *AJ*, 158, 144, doi: [10.3847/1538-3881/ab397d](https://doi.org/10.3847/1538-3881/ab397d)
- Kirk, J., Wheatley, P. J., Louden, T., et al. 2017, *MNRAS*, 468, 3907, doi: [10.1093/mnras/stx752](https://doi.org/10.1093/mnras/stx752)
- . 2018, *MNRAS*, 474, 876, doi: [10.1093/mnras/stx2826](https://doi.org/10.1093/mnras/stx2826)
- Kirk, J., Rackham, B. V., MacDonald, R. J., et al. 2021, *AJ*, 162, 34, doi: [10.3847/1538-3881/abfcd2](https://doi.org/10.3847/1538-3881/abfcd2)
- Kluyver, T., Ragan-Kelley, B., Pérez, F., et al. 2016, in *Positioning and Power in Academic Publishing: Players, Agents and Agendas*, ed. F. Loizides & B. Schmidt, IOS Press, 87 – 90
- Kreidberg, L. 2015, *PASP*, 127, 1161, doi: [10.1086/683602](https://doi.org/10.1086/683602)
- Kreidberg, L., Bean, J. L., Désert, J.-M., et al. 2014a, *Nature*, 505, 69, doi: [10.1038/nature12888](https://doi.org/10.1038/nature12888)
- . 2014b, *ApJL*, 793, L27, doi: [10.1088/2041-8205/793/2/L27](https://doi.org/10.1088/2041-8205/793/2/L27)
- Kreidberg, L., Line, M. R., Bean, J. L., et al. 2015, *ApJ*, 814, 66, doi: [10.1088/0004-637X/814/1/66](https://doi.org/10.1088/0004-637X/814/1/66)
- Kurucz, R.-L. 1993, *Kurucz CD-Rom*, 13
- Lecavelier Des Etangs, A., Pont, F., Vidal-Madjar, A., & Sing, D. 2008, *A&A*, 481, L83, doi: [10.1051/0004-6361:200809388](https://doi.org/10.1051/0004-6361:200809388)
- Lee, E. J., & Chiang, E. 2016, *ApJ*, 817, 90, doi: [10.3847/0004-637X/817/2/90](https://doi.org/10.3847/0004-637X/817/2/90)
- MacDonald, R. J., & Madhusudhan, N. 2019, *MNRAS*, 486, 1292, doi: [10.1093/mnras/stz789](https://doi.org/10.1093/mnras/stz789)
- Marsh, T. R. 1989, *Publications of the Astronomical Society of the Pacific*, 101, 1032, doi: [10.1086/132570](https://doi.org/10.1086/132570)
- McGruder, C. D., López-Morales, M., Espinoza, N., et al. 2020, *AJ*, 160, 230, doi: [10.3847/1538-3881/abb806](https://doi.org/10.3847/1538-3881/abb806)
- McGruder, C. D., López-Morales, M., Kirk, J., et al. 2022, *AJ*, 164, 134, doi: [10.3847/1538-3881/ac7f2e](https://doi.org/10.3847/1538-3881/ac7f2e)
- . 2023, *AJ*, 166, 120, doi: [10.3847/1538-3881/ace777](https://doi.org/10.3847/1538-3881/ace777)
- Mordasini, C., van Boekel, R., Mollière, P., Henning, T., & Benneke, B. 2016, *ApJ*, 832, 41, doi: [10.3847/0004-637X/832/1/41](https://doi.org/10.3847/0004-637X/832/1/41)

- Mortier, A., Santos, N. C., Sousa, S. G., et al. 2013, *A&A*, 558, A106, doi: [10.1051/0004-6361/201322240](https://doi.org/10.1051/0004-6361/201322240)
- Nikolov, N., Sing, D. K., Gibson, N. P., et al. 2016, *ApJ*, 832, 191, doi: [10.3847/0004-637X/832/2/191](https://doi.org/10.3847/0004-637X/832/2/191)
- Nikolov, N., Sing, D. K., Pont, F., et al. 2014, *MNRAS*, 437, 46, doi: [10.1093/mnras/stt1859](https://doi.org/10.1093/mnras/stt1859)
- Nikolov, N., Sing, D. K., Fortney, J. J., et al. 2018, *Nature*, 557, 526, doi: [10.1038/s41586-018-0101-7](https://doi.org/10.1038/s41586-018-0101-7)
- Nikolov, N. K., Sing, D. K., Spake, J. J., et al. 2022, *MNRAS*, 515, 3037, doi: [10.1093/mnras/stac1530](https://doi.org/10.1093/mnras/stac1530)
- Öberg, K. I., Murray-Clay, R., & Bergin, E. A. 2011, *ApJL*, 743, L16, doi: [10.1088/2041-8205/743/1/L16](https://doi.org/10.1088/2041-8205/743/1/L16)
- Pandas Development Team, T. 2020, *pandas-dev/pandas: Pandas, latest*, Zenodo, doi: [10.5281/zenodo.3509134](https://doi.org/10.5281/zenodo.3509134)
- Pollack, J. B., Hubickyj, O., Bodenheimer, P., et al. 1996, *Icarus*, 124, 62, doi: [10.1006/icar.1996.0190](https://doi.org/10.1006/icar.1996.0190)
- Pont, F., Sing, D. K., Gibson, N. P., et al. 2013, *MNRAS*, 432, 2917, doi: [10.1093/mnras/stt651](https://doi.org/10.1093/mnras/stt651)
- Rackham, B., Espinoza, N., Apai, D., et al. 2017, *ApJ*, 834, 151, doi: [10.3847/1538-4357/aa4f6c](https://doi.org/10.3847/1538-4357/aa4f6c)
- Rathcke, A. D., MacDonald, R. J., Barstow, J. K., et al. 2021, *AJ*, 162, 138, doi: [10.3847/1538-3881/ac0e99](https://doi.org/10.3847/1538-3881/ac0e99)
- Rathcke, A. D., Buchhave, L. A., Mendonça, J. M., et al. 2023, *MNRAS*, 522, 582, doi: [10.1093/mnras/stad1010](https://doi.org/10.1093/mnras/stad1010)
- Rothman, L. S., Gordon, I. E., Barber, R. J., et al. 2010, *JQSRT*, 111, 2139, doi: [10.1016/j.jqsrt.2010.05.001](https://doi.org/10.1016/j.jqsrt.2010.05.001)
- Rothman, L. S., Gordon, I. E., Babikov, Y., et al. 2013, *JQSRT*, 130, 4, doi: [10.1016/j.jqsrt.2013.07.002](https://doi.org/10.1016/j.jqsrt.2013.07.002)
- Rustamkulov, Z., Sing, D. K., Mukherjee, S., et al. 2023, *Nature*, 614, 659, doi: [10.1038/s41586-022-05677-y](https://doi.org/10.1038/s41586-022-05677-y)
- Sing, D. K., Pont, F., Aigrain, S., et al. 2011, *MNRAS*, 416, 1443, doi: [10.1111/j.1365-2966.2011.19142.x](https://doi.org/10.1111/j.1365-2966.2011.19142.x)
- Sing, D. K., Lecavelier des Etangs, A., Fortney, J. J., et al. 2013, *MNRAS*, 436, 2956, doi: [10.1093/mnras/stt1782](https://doi.org/10.1093/mnras/stt1782)
- Sing, D. K., Fortney, J. J., Nikolov, N., et al. 2016, *Nature*, 529, 59, doi: [10.1038/nature16068](https://doi.org/10.1038/nature16068)
- Sing, D. K., Lavvas, P., Ballester, G. E., et al. 2019, *AJ*, 158, 91, doi: [10.3847/1538-3881/ab2986](https://doi.org/10.3847/1538-3881/ab2986)
- Speagle, J. S. 2020, *Monthly Notices of the Royal Astronomical Society*, 493, 3132–3158, doi: [10.1093/mnras/staa278](https://doi.org/10.1093/mnras/staa278)
- Sromovsky, L. A., Fry, P. M., & Kim, J. H. 2011, *Icarus*, 215, 292, doi: [10.1016/j.icarus.2011.06.024](https://doi.org/10.1016/j.icarus.2011.06.024)
- Stevenson, K. B., Bean, J. L., Seifahrt, A., et al. 2016, *ApJ*, 817, 141, doi: [10.3847/0004-637X/817/2/141](https://doi.org/10.3847/0004-637X/817/2/141)
- Tashkun, S. A., & Perevalov, V. I. 2011, *JQSRT*, 112, 1403, doi: [10.1016/j.jqsrt.2011.03.005](https://doi.org/10.1016/j.jqsrt.2011.03.005)
- Tremblin, P., Amundsen, D. S., Chabrier, G., et al. 2016, *ApJL*, 817, L19, doi: [10.3847/2041-8205/817/2/L19](https://doi.org/10.3847/2041-8205/817/2/L19)
- Tremblin, P., Amundsen, D. S., Mourier, P., et al. 2015, *ApJL*, 804, L17, doi: [10.1088/2041-8205/804/1/L17](https://doi.org/10.1088/2041-8205/804/1/L17)
- Underwood, D. S., Tennyson, J., Yurchenko, S. N., et al. 2016, *MNRAS*, 459, 3890, doi: [10.1093/mnras/stw849](https://doi.org/10.1093/mnras/stw849)
- Vidal-Madjar, A., Lecavelier des Etangs, A., Désert, J. M., et al. 2003, *Nature*, 422, 143, doi: [10.1038/nature01448](https://doi.org/10.1038/nature01448)
- Virtanen, P., Gommers, R., Oliphant, T. E., et al. 2020, *Nature Methods*, 17, 261, doi: [10.1038/s41592-019-0686-2](https://doi.org/10.1038/s41592-019-0686-2)
- Vissapragada, S., Knutson, H. A., Greklek-McKeon, M., et al. 2022, *AJ*, 164, 234, doi: [10.3847/1538-3881/ac92f2](https://doi.org/10.3847/1538-3881/ac92f2)
- Wakeford, H. R., Sing, D. K., Evans, T., Deming, D., & Mandell, A. 2016, *ApJ*, 819, 10, doi: [10.3847/0004-637X/819/1/10](https://doi.org/10.3847/0004-637X/819/1/10)
- Wakeford, H. R., Visscher, C., Lewis, N. K., et al. 2017a, *MNRAS*, 464, 4247, doi: [10.1093/mnras/stw2639](https://doi.org/10.1093/mnras/stw2639)
- Wakeford, H. R., Sing, D. K., Deming, D., et al. 2013, *MNRAS*, 435, 3481, doi: [10.1093/mnras/stt1536](https://doi.org/10.1093/mnras/stt1536)
- Wakeford, H. R., Stevenson, K. B., Lewis, N. K., et al. 2017b, *ApJL*, 835, L12, doi: [10.3847/2041-8213/835/1/L12](https://doi.org/10.3847/2041-8213/835/1/L12)
- Wakeford, H. R., Sing, D. K., Kataria, T., et al. 2017, *Science*, 356, 628–631, doi: [10.1126/science.aah4668](https://doi.org/10.1126/science.aah4668)
- Wakeford, H. R., Sing, D. K., Deming, D., et al. 2018, *AJ*, 155, 29, doi: [10.3847/1538-3881/aa9e4e](https://doi.org/10.3847/1538-3881/aa9e4e)
- Weaver, I. C., López-Morales, M., Espinoza, N., et al. 2020, *AJ*, 159, 13, doi: [10.3847/1538-3881/ab55da](https://doi.org/10.3847/1538-3881/ab55da)
- Weaver, I. C., López-Morales, M., Alam, M. K., et al. 2021, *AJ*, 161, 278, doi: [10.3847/1538-3881/abf652](https://doi.org/10.3847/1538-3881/abf652)
- Wes McKinney. 2010, in *Proceedings of the 9th Python in Science Conference*, ed. Stéfan van der Walt & Jarrod Millman, 56 – 61, doi: [10.25080/Majora-92bf1922-00a](https://doi.org/10.25080/Majora-92bf1922-00a)
- Wong, I., Benneke, B., Gao, P., et al. 2020, *AJ*, 159, 234, doi: [10.3847/1538-3881/ab880d](https://doi.org/10.3847/1538-3881/ab880d)
- Yurchenko, S. N., Barber, R. J., & Tennyson, J. 2011, *MNRAS*, 413, 1828, doi: [10.1111/j.1365-2966.2011.18261.x](https://doi.org/10.1111/j.1365-2966.2011.18261.x)
- Yurchenko, S. N., & Tennyson, J. 2014, *MNRAS*, 440, 1649, doi: [10.1093/mnras/stu326](https://doi.org/10.1093/mnras/stu326)